Research Article | Vol. 30, No. 4 / 14 Feb 2022 / Optics Express 5008
Optics EXPRESS

Two-dimensional multi-layered SiN-on-SOI optical phased array with wide-scanning and long-distance ranging

LANXUAN ZHANG,[1] YINGZHI LI,[1] BOSONG CHEN,[1] YUBING WANG,[2] HONGMEI LI,[1] YU HOU,[1] MIN TAO,[1] YUXUAN LI,[1] ZIHAO ZHI,[1] XIAOBIN LIU,[1] XUETONG LI,[1] QUANXIN NA,[3] QIJIE XIE,[3] MINGSHI ZHANG,[2] XUEYAN LI,[1,3] FENGLI GAO,[1] XIANSHU LUO,[4] GUO-QIANG LO,[4] AND JUNFENG SONG[1,3,*]

[1]*State Key Laboratory of Integrated Optoelectronics, College of Electronic Science and Engineering, Jilin University, Changchun 130012, China*
[2]*State Key Laboratory of Luminescence and Application, Changchun Institute of Optics, Fine Mechanics and Physics, Chinese Academy of Sciences, Changchun 130010, China*
[3]*Peng Cheng Laboratory, Shenzhen 518000, China*
[4]*Advance Micro Foundry Pte Ltd, 11 Science Park Road, Singapore Science Park II, Singapore 117685, Singapore*
[*]*songjf@jlu.edu.cn*

Abstract: Silicon based optoelectronic integrated optical phased array is attractive owing to large-dense integration, large scanning range and CMOS compatibility. In this paper, we design and fabricate a SiN-on-SOI two-dimensional optical phased array chip. We demonstrate a two-dimensional scanning range of 96°×14.4° and 690 mW peak power of the main lobe. Additionally, we set up the time of flight (ToF) and frequency-modulated continuous-wave (FMCW) ranging systems by using this optical phased array chip, and achieve the objects detection at the range of 20 m in the ToF system and 109 m in the FMCW system, respectively.

1. Introduction

Optical phased arrays (OPAs) [1–4] have been recently proposed as a promising solid state technology to achieve fully integrated and cheap LiDAR sensing on silicon photonics chips. OPAs have been utilized successfully for beam scanning, object imaging [5,6], ranging detection and optical communication [7–11] in chip level. Each waveguide of optical phased array is equivalent to a single slot in the multi-slots Fraunhofer diffraction. By modulating the phase of each waveguide, the wave front of incident light will be directed to different direction for horizontal scanning [12]. There are two common methods to realize the two-dimensional steering of the OPA. The one is a two-dimensional grating coupler matrix constituted by M×N phase shifters [4,13]. By controlling the phase difference among the phase shifters, two directional beam steering can be achieved. The other way is the grating coupler etched on waveguide [14–16]. Vertical scanning is achieved by adjusting the wavelength of the incident light, and horizontal scanning is performed through the phase shifting. The number of phase shifters in the latter structure is only N, which greatly reduces the complexity of chip manufacturing.

For range measurement, high-power signal can be beneficial to high signal-to-noise ratio(SNR), and thus long detection range [17]. Therefore, the damage threshold of the OPA is a critical figure of merit for LiDAR application. Si is a common waveguide material using in the OPAs, but the damage threshold is limited by the two-photon absorption effect [18]. On the contrary, integrated devices based on silicon nitride (SiN) have become a powerful alternative to silicon devices due to their low nonlinearity, wide transparency range, low transmission loss and low refractive index

#446733 https://doi.org/10.1364/OE.446733
Journal © 2022 Received 25 Oct 2021; revised 22 Jan 2022; accepted 25 Jan 2022; published 2 Feb 2022

Optics EXPRESS

contrast [19]. Until now, several SiN-based OPAs have been investigated, but the beam steering range is limited [20–22]. Compared to the SiN-based modulator, the thermo-optical coefficient of Si-based modulator is one order of magnitude higher. Therefore, Si material is a potential choice for phase modulator. Moreover, Si waveguides exhibit superior performance as grating antennas by allowing smaller bending radius without significantly increasing the transmission loss. So far, several OPA chips have adopted the integration of SiN and Si [23,24]. However, the power analysis and range measurement of the SiN-Si hybrid OPA chip is seldom reported.

In this article, we report a 64-channel two-dimensional SiN-on-SOI OPA chip which has a wide scanning field of view and high optical power handling capability for long-distance ranging. The OPA is constituted by SiN-based coupler, SiN-based beam splitter and Si-based phase shifter, with a total loss of about 12.5 dB. The two-dimension steering range of 96°×14.4° is demonstrated by combining phase tuning and wavelength tuning. To realize time-of-flight (ToF) ranging, we investigate the relation between the main lobe power of the two-dimensional chip and the power of input pulsed laser, the maximum peak power of the main lobe is up to 690 mW. Consequently, the OPA chip is used to successfully achieve a long range detection with up to 20 meters distance in the ToF system by using a 10-ns width pulsed laser at the 100 kHz repetition rate. In addition, we also demonstrate the range measurement by using the OPA chip in the frequency modulated continuous wave (FMCW) system, with a detection range of up to 109 m.

2. Design and fabrication

In order to improve the damage threshold of the chip, the waveguides and devices on the front end of the chip are fabricated by the SiN [18]. The laser beam from the lensed fiber is coupled into the SiN waveguide via spot-size converter (SSC), which is an adiabatic waveguide of 200 μm in length with the width tapering from 0.4 μm to 1.5 μm. Subsequently, the light is divided into 64 channels by the 6-level Y splitter and coupled into the Si waveguide through a SiN-to-Si tapered coupler [25]. The inter-layer coupler we use is illustrated in Fig. 1(c). Tt shows the width of SiN and Si waveguide at the start of the coupler, and the inter-layer coupling length is 150 μm. The phase modulation is released through thermo-optic tunable waveguides. The width of the Si waveguide is 450 nm, and the spacing between two adjacent waveguides is 5 μm. At the end of the chip, the spacing is reduced from 5 μm to 1 μm. The grating period etched in the Si waveguide is 820 nm. Figure 1(a) shows the optical microscope image of the fabricated OPA. The chip is fabricated on Silicon-On-Insulator (SOI) with 220-nm silicon layer and 3 μm BOX layer. Figure 1(b) shows the cross-sectional view of the design and the relative height of each

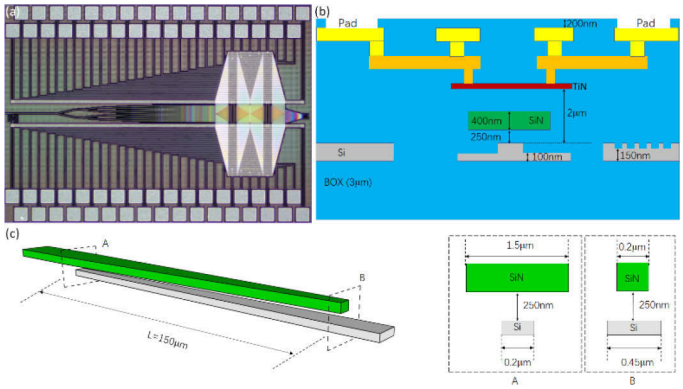

Fig. 1. (a) Optical microscope picture of the OPA. (b)The structure and relative dimension of each layer of the chip. (c) Schematic of the inter-layer transition.

Optics EXPRESS

layer. The SiN waveguide is with thickness of 400 nm through Plasma-enhanced chemical vapor deposition (PECVD). The TiN is used as the thermal heaters, and Al is used as the routing metal.

3. Experimentation

3.1. Experimental setup

Figure 2(a) and 2(b) show the block diagram of the experimental system and the actual set up for the beam steering. The whole system consists of the upper computer control, the power supply, the chip under test, and the observation screen. The lensed fiber is well packaged to the waveguide and the chip is bonded on the PCB connected by 64 voltage sources. In order to capture the far-field beam of the two-dimensional OPA, the chip is placed vertically so that the far-field beam is directly irradiated on the observation screen. The observation screen is 6 cm away from the chip, and the scale is marked in the unit of millimeters. The upper computer is used to control the voltage source by calculating the far-field intensity information. The entire system workflow is shown in Fig. 2(c). Firstly, we initialize the parameters, including the step voltage value, V_{step}, the maximum voltage value, V_{max}, and the number of scanning starting channel, i. Then the upper computer controls the voltage source to increase the voltage of the i-th circuit from 0 in order to modulate the phase. Each time when the voltage value is increased, the upper computer software extracts the intensity distribution of the far-field image under this voltage, comparing with the pre-stored ideal intensity distribution, and calculates the similarity. Then the upper computer selects the voltage value corresponding to the maximum similarity as the voltage value required for the i-th phase modulation. We perform the aforementioned operations step by step for each individual channel until the voltage of the 64 power sources is determined, and the most ideal far-field distribution is obtained. Finally, the group of 64 voltage values is stored for subsequent configuration. For each scanning angle, we have to repeat the phase calibration process [14].

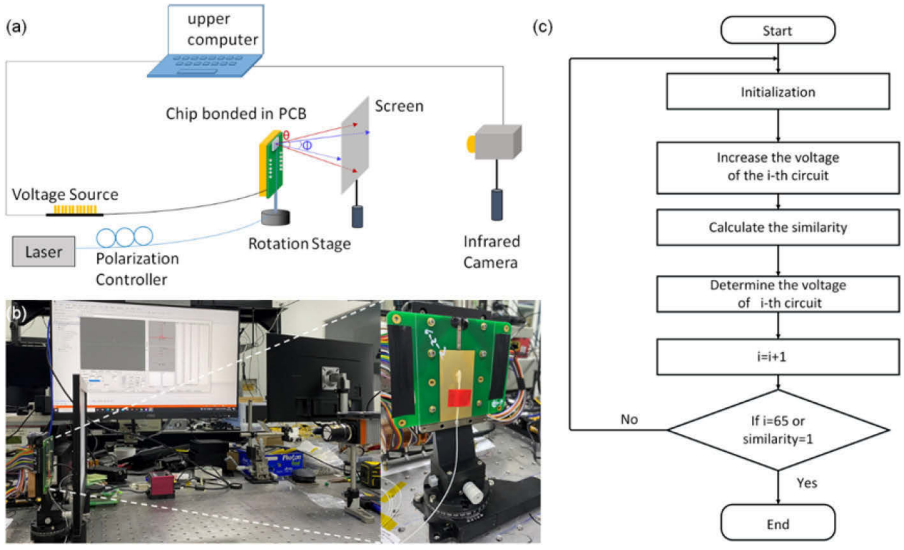

Fig. 2. (a) The block diagram the experimental system. (b) The actual setup for beam positioning. (c) The entire system workflow for phase calibration.

Optics EXPRESS

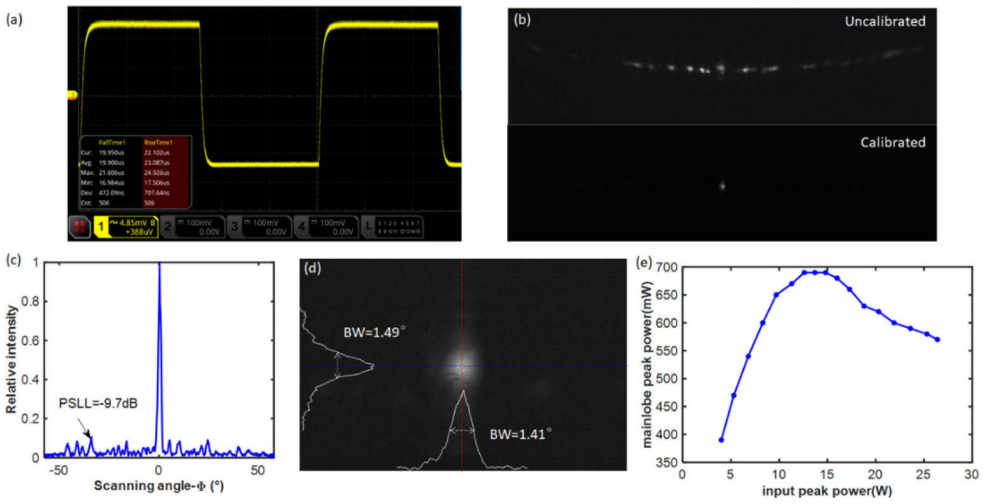

Fig. 3. (a) Oscilloscope screenshot of the transmitted NRZ signal from the MZI. (b) Far-field images before and after phase calibration. (c) Intensity distribution of 0°beam. (d) The main lobe spot at 50 cm away. (e) The main lobe power upon different input powers.

3.2. Scanning performance

The horizontal dimension is usually controlled by adjusting the phase difference between the waveguides. We measure the phase shift properties of the thermo-optic phase modulation structure by using a Mach–Zehnder interferometer (MZI). The heater in one arm is driven by a 1 kHz square voltage signal, the thermo-optical switch shows $t_{rise} = 23.1$ µs and $t_{fall} = 19.9$ µs as shown in Fig. 3(a). The laser in TE-polarization is coupled into the chip, and subsequently enters 64 optical waveguides through multi-staged Y-splitter. Due to the random phase difference in each waveguide, the output light fails to constructively interfere in a certain direction of the far field. Hence, no obvious main lobe can be observed as shown in the upper figure of Fig. 3(b). In contrast, the measured beam profile at 0° after the phase calculation is shown in the bottom in Fig. 3(b). The extracted intensity distribution is shown in Fig. 3(c). It can be seen that the peak-side-lobe level is −9.7 dB. Figure 3(d) shows the main lobe spot at 50 cm away, with a transverse divergence angle of 1.41° and a longitudinal divergence angle of 1.49°. When the incident power is 0.84 mW, the measured main lobe power is about 47 µW and thus the total loss is about 12.5 dB. The loss includes 1.8 dB fiber to chip coupling loss, 2 dB loss in Y-beam splitting network, 0.2 dB SiN-Si coupling loss and about 8.5 dB antenna transmission loss. A pulsed laser with pulse width of 10 ns and repetition rate of 100 kHz is used as a light source of the OPA. The relationship between main lobe power and input power is shown in Fig. 3(e). The power of main lobe increases firstly and then drops as the input power increased. The reason for the decrease is the two-photon absorption effect of Si optical waveguide as analyzed in [18], which limits the continuous increase of main lobe. The maximum peak power of main lobe of the chip can reach up to 690 mW.

The phase of the scanning beams with different scanning angles is calibrated to obtain the horizontal scanning image of the chip. Figure 4(a) shows the far-field image observed by the camera when the observation screen is placed 6 cm away from the chip. We obtain the scanning beams in the horizontal range of −47° ~ 49°. In order to extract the intensity distribution of beams at different angles more accurately, we rotate the chip to aim the different beams at the center of the observation screen. It is equivalent to rotating the camera to collect beams of different angles. The intensity distribution of the beam at different angles extracted by this method is shown in

Optics EXPRESS

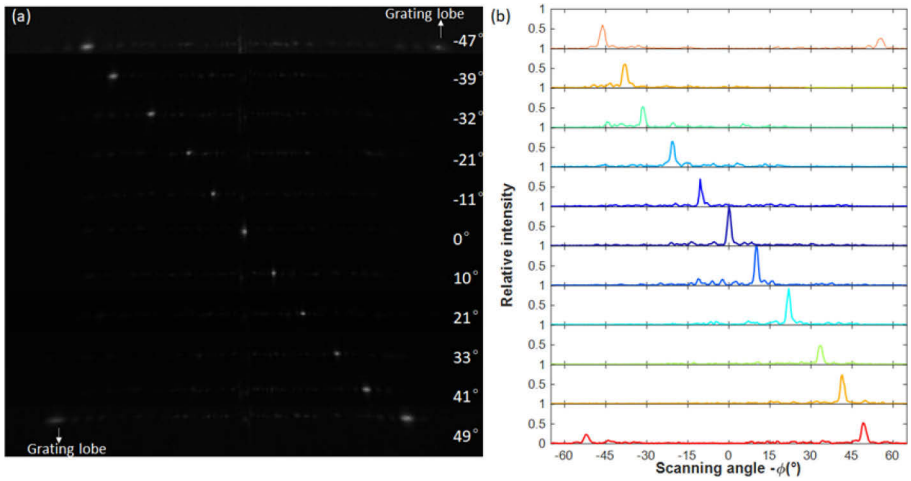

Fig. 4. (a) Far-field of the OPA in horizontal direction. (b) Gray distribution of scanning beams.

Fig. 4(b). It can be seen from the far-field image that grating lobe appears at −52°, when the scanning beam is pointed at 49°. As the scanning beam is pointed at −47°, grating lobe appears at 55°. The interval between the two grating lobes was 101° and 102° respectively. For uniformly OPA, the interval between the two grating lobes is determined by $\Delta\theta = 2\arcsin(0.5\lambda/d)$, where λ is the laser wavelength, d is the waveguide spacing. For our chip with equal spacing of 1 μm, the theoretical spacing between the two grating lobes is 101.6°. The discrepancy between the theoretical and measured results can be attributed to the positioning error caused by the rotation accuracy of the rotary stage. Each scanning beam corresponds to a set of configuration voltages and the averaged electric power required for each steering is 1.33 W.

The beam steering along vertical dimension can be achieved by tuning the wavelength of incident light. For a single waveguide grating antenna, the longitudinal radiation angle can be estimated by the following equation based on diffraction theory [26], where θ is the angle between the radiation direction of the beam and the normal direction of the grating:

$$\sin\theta = n_{eff} - \frac{\lambda_0}{\Lambda} \tag{1}$$

where Λ is the period of grating, n_{eff} is the effective refractive index of the grating, λ_0 is the wavelength of the input laser.

Figure 5(a) shows the schematic view of the waveguide grating. In the grating region, the waveguide width is 400 nm, the etched depth is 70 nm and the duty cycle is 50%. We use Lumerical Finite Difference Time Domain (FDTD) tools to simulate the emission of grating. When the incident laser is from 1540 nm to 1630 nm, the normalized emission intensity in the far-field is shown in Fig. 5(b), the transverse angle is zero, i.e. $\phi = 0°$ in this case. It can be seen that the far-field scanning angle decreases with the increase of incident wavelength. Figure 5(c) shows the relationship between specific wavelength and emission angle, when the wavelength is tuned within 1540–1630 nm, the diffraction angle is from 10.4° to −3.17°, the scanning range can reach 13.47°. For the light with 1550 nm wavelength, we can get from the simulation that the longitudinal beam divergence is 1.9°. The total grating area length is 82 μm. The grating is with constant perturbations, it emits an exponential profile, therefore, the actual grating length is less than 82 μm. Figure 5(d) shows the power transmission in five equidistant waveguides whose length is 82 μm, the space is 1μm. The light is incident from the central waveguide. The results show that about 4% of the power is coupled to the adjacent waveguide when the light travels the

Optics EXPRESS

distance of 41μm (dotted line). The inset shows the near-field intensity distribution of the actual grating, we can see that when the light propagates 41 μm, the diffraction intensity has decreased to about 20%. Therefore, 4% of the coupling power between waveguides can be ignored in this grating.

Prior to the wavelength tuning, we fix the horizontal angle at φ=0°.The longitudinal steering situation is shown in Fig. 6. Figure 6(a) shows the far-field image observed by the infrared camera when the wavelength is adjusted from 1540 nm to 1630 nm. The longitudinal intensity distribution of the beams corresponding to different wavelengths is extracted as shown in Fig. 6(b).

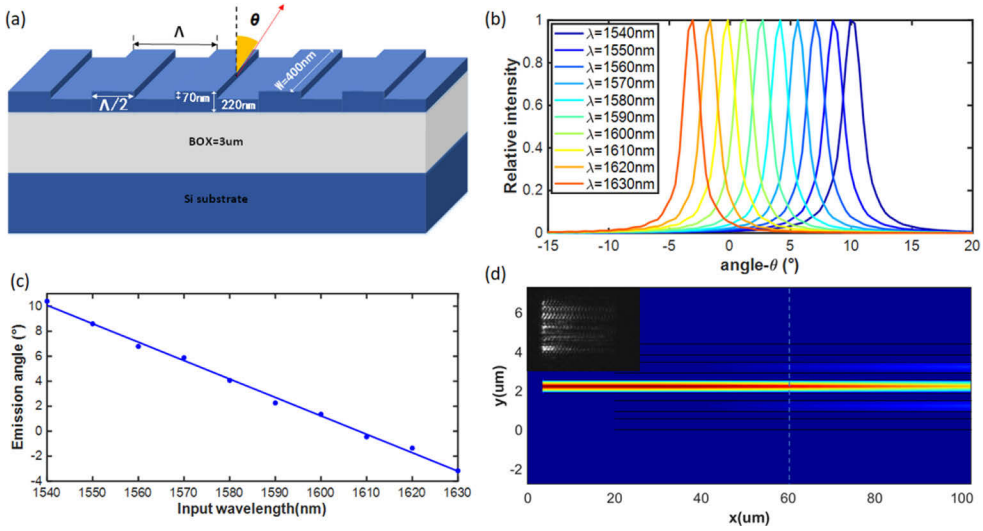

Fig. 5. (a) The schematic view of the waveguide grating. (b) The normalized emission intensity in the far-field in different wavelength. (c) The relationship between specific wavelength and emission angle. (d) The power transmission in equidistant waveguides.

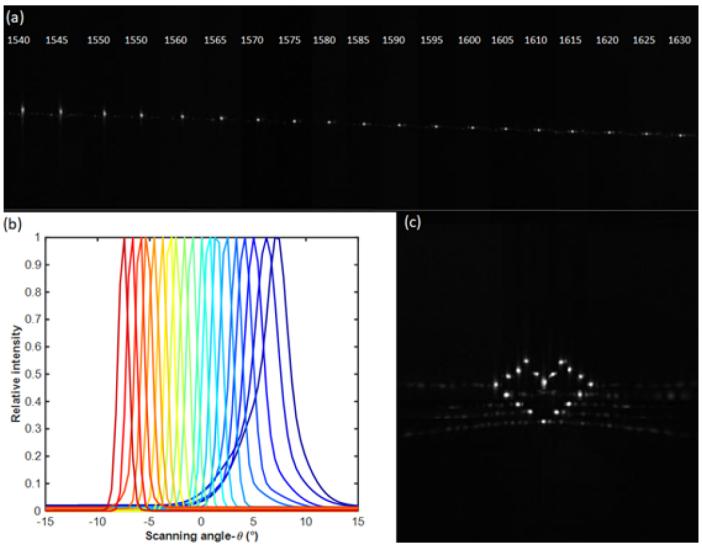

Fig. 6. (a) Far-field of the OPA in vertical direction. (b) Gray distribution of scanning beams (c) The heart-shaped pattern scanning by this chip.

Optics EXPRESS

The longitudinal steering of 14.4° is realized. The scanning range is close to the above simulation results, but the diffraction angle corresponding to different wavelengths is smaller than the simulation. This is due to the manufacturing error of the waveguide, which has been analyzed in detail in our previous work [27]. Utilizing the two-dimensional scanning capability of the chip, we successfully scan a heart-shaped pattern in the far-field, as shown in Fig. 6(c).

4. Ranging detection with optical phased array

4.1. Time of flight LiDAR

The principle of ToF (Time of Flight) is shown in Fig. 7(a). The light source emits pulse laser light and the reflected light is received by a detector. The distance of the measured object can be estimated by $L = C \times \Delta t/2$.The power of two-dimensional 64-channel SiN-Si hybrid OPA has been analyzed above. We set up a ToF ranging system with this chip as shown in Fig. 7(b). The pulse laser with pulse width of 10 ns is used as the source of the OPA and coupled into the chip through the polarization controller. Finally, the main lobe of the OPA is used to detect the object. The reflector with 90% reflectivity indicated by the red arrow on the right side of Fig. 7(b) is used as the target. The reflected light enters the APD, and the pulse signal received by the APD is displayed by oscilloscope and the receiving time is calculated. Different receiving times correspond to different distances. The resolution of the ToF system is linked to the pulse width of the signal τ_{3dB}: $\Delta d = C\tau_{3dB}$, therefore, the resolution of this system is 3 m.

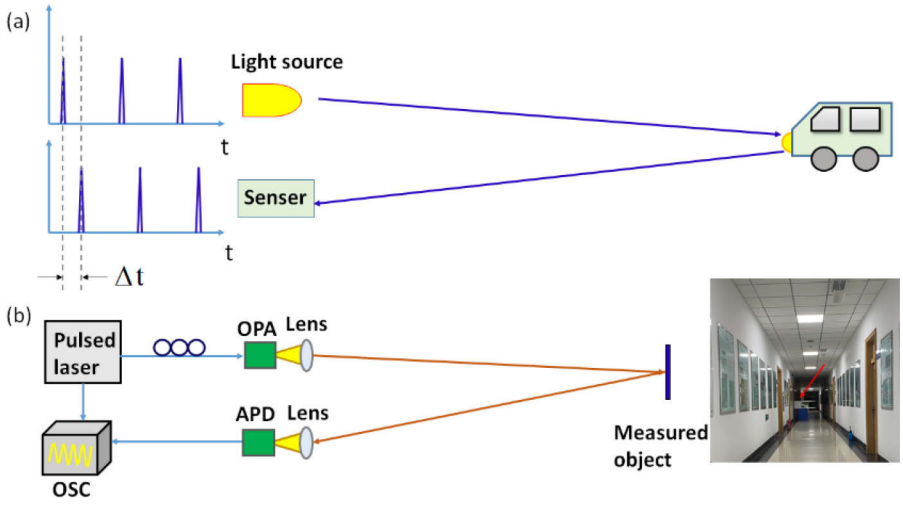

Fig. 7. (a) The principle of time of flight detection. (b) ToF (Time of Flight) ranging system with this chip

Firstly, we investigate the maximum ranging distance of the system without lens in front of the chip, and the results show that the ranging limit is only 4 m in this case. In order to improve the detection ability of the system, we place a lens in front of the chip to concentrate the main lobe power. The objects are placed at different distances for detection. The distances of these positions are calibrated by the rangefinder (Deli DL4171) as follows: 4.993 m, 7.519 m, 10.822 m, 15.066 m, 17.586 m and 20.252 m. Figure 8(a) shows the received signal of the APD when the target is placed at different positions. After normalizing the received signal, the peak side lobe level PSLL of the received signal is calculated and defined as the received signal quality. The peak and signal quality of the received signal at different positions are plotted Fig. 8(b), they decrease as the increase of distance. When the targeted object is placed at 20.252 m, the signal received by the APD is very weak, and the SNR reduces 10.5 dB to 2.2 dB. Therefore, the OPA

Optics EXPRESS

ranging can be measured is limited at 20.252 meters. In total, we completed 100 measurements at each of the above last five positions. The standard deviations of the measurement results at different positions are respectively 14.1 cm, 12.8 cm, 21.2 cm, 29.8 cm and 34.6 cm. Taking the averaged value of the 100 measurement values as the result for every distance, Fig. 8(c) shows the relationship between the measured flight time and the actual distance. The measured time value has a very well linear relationship with the actual distance value. After fitting, the errors between the fitted distance value and the actual distance value (the accuracy) are as follows: 0.51 cm, 0.33 cm, 1.03 cm, 0.73 and 0.12 cm. We also explore the ranging capability of the edge 49° beam of the OPA, and we achieve the detection of the target at 14 m successfully. We place the target at the positions of 2.210 m, 5.010 m, 8.103 m, 11.310 m and 14.197 m. In total, we completed 100 measurements at each of the above last five positions. The standard deviations of the measurement results at different positions are respectively 3.9 cm, 5.8 cm, 10.3 cm, 18.1 cm and 26 cm. Figure 8(d) shows the relationship between the measured flight time and the actual distance. After fitting, we can get the accuracy are as follows: 7.5 cm, 7.2 cm, 3.4 cm, 0.6 cm, and 3.8 cm.

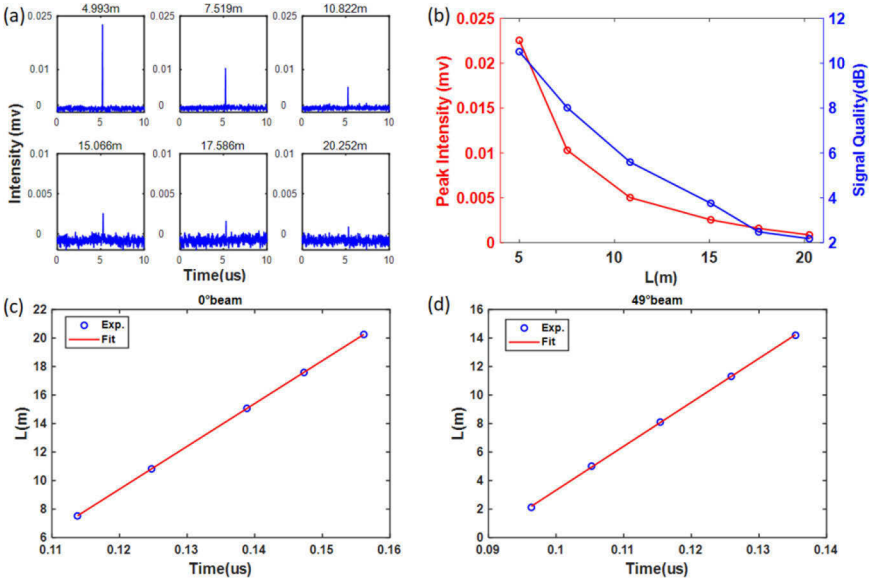

Fig. 8. (a) The received signal of APD when the reflector is placed at different positions. (b) The peak and signal quality of the received signal at different positions. (c) The relationship between the measured flight time and the actual distance of 0° beam. (d) The relationship between the measured flight time and the actual distance of 49° beam.

4.2. *Frequency-modulated continuous-wave (FMCW) LiDAR*

The ranging principle of FMCW coherent LiDAR is shown in Fig. 9(a). The frequency modulated laser is divided into two paths. One is used as a local light, while the other is used as a signal light. Beat signal is achieved by mixing the local light and reflected light. The frequency shift is calculated from the beat signal, and the distance will be obtained by analyze the frequency shift. The gradient of modulated frequency $Chirp = f_{DEV}/t_s$. Therefore, the range to target is $R = f_b/Chirp \times C \times 0.5 = f_b/f_{DEV} \times t_s \times C \times 0.5$, where f_b is the optical frequency difference between the transmitted and received signals, f_{dev} is the bandwidth of the laser being modulated, t_s is the time corresponding to the optical frequency scanning, and C is the speed of light. Since the f_{dev} and t_s are determined in the system, the detection distance is directly proportional to the

Optics EXPRESS

f_b. Figure 9(b) shows a block diagram of the entire FMCW LiDAR system with two-dimensional OPA. The resolution of the FMCW system is linked to the bandwidth of the modulation: $\Delta d = C/(2f_{DEV})$, the bandwidth of the laser in this system is 3 GHz, we can get the resolution of the FMCW system is 5 cm. The single frequency fiber laser is externally modulated by a 30 MHz/μs chirp signal and then amplified by an EDFA. Subsequently, the light is divided into two branches by a 10/90 directional coupler. The 10% power directly reaches the output 2×2 combiner, and the other 90% power is amplified by the second-level EDFA and going through the polarization controller and then enters the OPA. The light reflected by the object enters the collimating lens for the signal detection. The light goes through the 2×2 combiner and is detected by a balanced photodetector. The beat signal is captured by an oscilloscope. Due to the limited experimental conditions, the detection of objects at 100 m away is achieved by using a mirror to reflect the light back and forth. In this test system, the emitted light signal passes through the reflector at L_1 and is reflected from the measured object at L_2. The measured target is a reflector with a reflectivity of 90%, and the actual distance traveled by the light is $L_1 + L_2$.

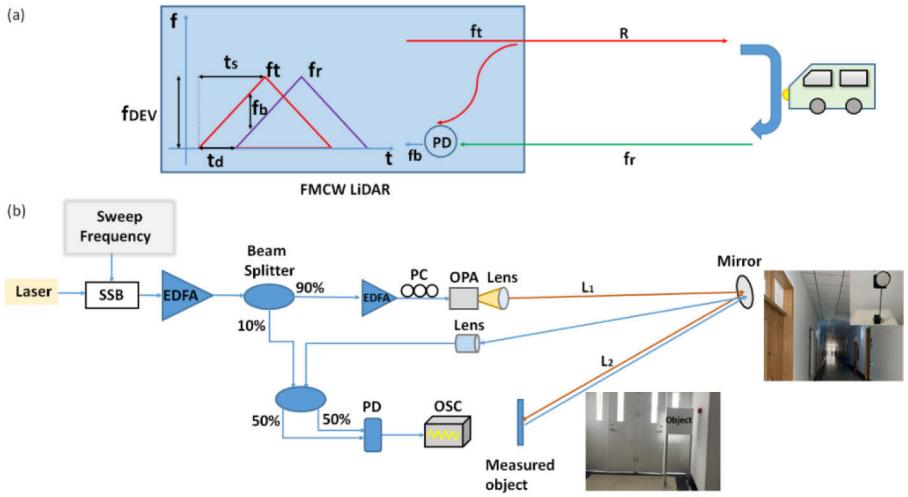

Fig. 9. (a) The principle of FMCW detection. (b) FMCW ranging system with this chip.

When there is no lens in front of the chip, the farthest detection distance of the system is 36 m. When we place the lens, the detection distance increases greatly. The beat signal is plotted in Fig. 10(a) with a range of 109 m. In the case of 90% reflectivity, the input power of the OPA decreases from 32 dBm to 26.5 dBm and the SNR of the beat signal decreases from 16.5 dB to 4.2 dB. In the case that the reflectivity of the target is only 10%, input power of the chip decreases from 32 dBm to 29 dBm and the SNR decreases from 8.4 dB to 3.4 dB. Further distance can be measured by using the OPA chip. In order to determine the accuracy of FMCW ranging, we measure five positions of 20.055 m, 30.213 m, 50.817 m, 80.278 m and 102.25 m. Each position is measured with 100 times. The standard deviations of the five positions are respectively 1.2 cm, 1.4 cm, 1.2 cm, 1.2 cm and 1.3 cm. They are much smaller than the standard deviation of those by ToF ranging. Similar to the analysis of ToF, we take the average value of 100 measured values as the result for every distance. Figure 10(b) shows the relationship between the measured beat frequency and the actual distance. After fitting, the errors between the fitted distance value and the actual distance value (the accuracy) are as follows: 1.9 cm, 0.8 cm, 1.4 cm, 2.2 cm and 0.9 cm. In the FMCW ranging system, we also investigate the ranging performance of 49° scanning beam. The results show that the edge scanning beam can still detect the object at the distance of 82 m. We measure five positions of 10.683 m, 25.161 m, 40.116 m, 51.434 m and 82.057

Optics EXPRESS

m. Each position is measured with 100 times. The standard deviations of the five positions are respectively 3.4 cm, 0.3 cm, 3.0 cm, 4.2 cm and 3.6 cm. Figure 10(c) shows the relationship between the measured beat frequency and the actual distance. After fitting, we can get the ranging accuracy in the above positions are :1.9 cm, 0.8 cm, 1.4 cm, 2.2 cm and 0.9 cm.

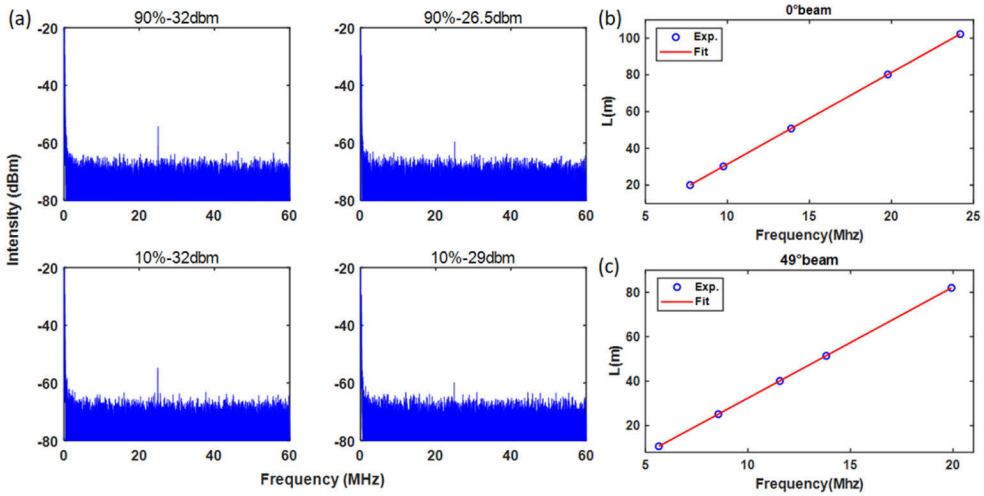

Fig. 10. (a) The received signal when the reflectivity of the object and the input power are different. (b) The relationship between the measured peak frequency and the actual distance of 0° beam. (c) The relationship between the measured peak frequency and the actual distance of 49° beam.

5. Conclusion

Combining the merits of high power handling capability of SiN waveguide and high thermo-optical modulation efficiency of Si waveguide, we achieved a wide-range and high-power SiN-on-Si 64-channel two-dimensional OPA. The field of view of the chip can reach 96°×14.4°, and a heart-shaped pattern was successfully scanned in the far field. Range detections by using the OPA chip were experimentally demonstrated. The detection of object at the range of 20 m and 109 m in the ToF and the FMCW system were realized respectively.

Funding. National Natural Science Foundation of China (61627820, 61934003, 62090054, 62105173, 62105174); Major scientific and technological program of Jilin Province (20200501007GX); Program for Jilin University Science and Technology Innovative Research Team (JLUSTIRT, 2021TD-39); Basic and Applied Basic Research Foundation of Guangdong Province (2019A1515111206).

Acknowledgments. We thank Prof. Liu-Qiang Zhang in Chongqing University for spice simulation.

Disclosures. The authors declare that there are no conflicts of interest related to this article.

Data availability. Data underlying the results presented in this paper are not publicly available at this time but may be obtained from the authors upon reasonable request.

References

1. V. A. Karel, B. Wim, J. Jana, L. T. Nicolas, H. Romuald, and B. Roel, "Off-chip beam steering with a one-dimensional optical phased array on silicon-on-insulator," Opt. Lett. **34**(9), 1477–1479 (2009).
2. V. A. Karel, R. Hendrik, and B. Roel, "Two-dimensional optical phased array antenna on silicon-on-insulator," Opt. Express **18**(13), 13655–13660 (2010).
3. D. Kwong, A. Hosseini, Y. Zhang, and R. T. Chen, "1 × 12 Unequally spaced waveguide array for actively tuned optical phased array on a silicon nanomembrane," Appl. Phys. Lett. **99**(5), 051104 (2011).
4. J. Sun, E. Timurdogan, A. Yaacobi, E. S. Hosseini, and M. R. Watts, "Large-scale nanophotonic phased array," Nature **493**(7431), 195–199 (2013).

Optics EXPRESS

5. F. Aflatouni, B. Abiri, A. Rekhi, and A. Hajimiri, "Nanophotonic coherent imager," Opt. Express **23**(4), 5117–5125 (2015).
6. H. A. Clevenson, S. J. Spector, L. Benney, M. G. Moebius, J. Brown, A. Hare, A. Huang, J. Mlynarczyk, C. V. Poulton, E. Hosseini, M. R. Watts, R. Dawson, J. P. Laine, and B. F. Lane, "Incoherent light imaging using an optical phased array," Appl. Phys. Lett. **116**(3), 031105 (2020).
7. H. Elgala, R. Mesleh, and H. Haas, "High-Speed Wireless Communication using Beam Steering by Optical Phased Array in Silicon," IEEE Commun. Mag. **49**(9), 56–62 (2011).
8. H.-W. Rhee, J.-B. You, H. Yoon, K. Han, M. Kim, B. G. Lee, S.-C. Kim, and H.-H. Park, "32 Gbps Data Transmission With 2D Beam-Steering Using a Silicon Optical Phased Array," IEEE Photonics Technol. Lett. **32**(13), 803–806 (2020).
9. C. V. Poulton, A. Yaacobi, Z. Su, M. J. Byrd, and M. R. Watts, "Optical Phased Array with Small Spot Size, High Steering Range and Grouped Cascaded Phase Shifters," in *Advanced Photonics 2016 (IPR, NOMA, Sensors, Networks, SPPCom, SOF), OSA technical Digest (online)* (Optical Society of America, 2016), paper IW1B.2.
10. W. S. Rabinovich, P. G. Goetz, M. W. Pruessner, R. Mahon, M. S. Ferraro, D. Park, E. Fleet, and M. J. DePrenger, "Two-dimensional beam steering using a thermo-optic silicon photonic optical phased array," Opt. Eng. **55**(11), 111603 (2016).
11. D. V. Christopher V, Ehsan Hosseini Poulton, Z. S. Erman Timurdogan, Benjamin Moss, and Michael R. Watts, "Lens-Free Chip-to-Chip Free-Space Laser Communication Link with a Silicon Photonics Optical Phased Array," in *Frontiers in Optics 2017, OSA Technical Digest (online)* (Optical Society of America, 2017), paper FW5A.3.
12. D. Zhuang, L. Zhagn, X. Han, Y. Li, Y. Li, X. Liu, F. Gao, and J. Song, "Omnidirectional beam steering using aperiodic optical phased array with high error margin," Opt. Express **26**(15), 19154–19170 (2018).
13. J. Sun, E. Hosseini, A. Yaacobi, D. B. Cole, G. Leake, D. Coolbaugh, and M. R. Watts, "Two-dimensional apodized silicon photonic phased arrays," Opt. Lett. **39**(2), 367–370 (2014).
14. J. K. Doylend, M. J. R. Heck, J. T. Bovington, J. D. Peters, L. A. Coldren, and J. E. Bowers, "Two-dimensional free-space beam steering with an optical phased array on silicon-on-insulator," Opt. Express **19**(22), 21595–21604 (2011).
15. D. Kwong, A. Hosseini, J. Covey, Y. Zhang, X. Xu, H. Subbaraman, and R. T. Chen, "On-chip silicon optical phased array for two-dimensional beam steering," Opt. Lett. **39**(4), 941–944 (2014).
16. D. N. Hutchison, J. Sun, J. K. Doylend, R. Kumar, J. Heck, W. Kim, C. T. Phare, A. Feshali, and H. Rong, "High-resolution aliasing-free optical beam steering," Optica **3**(8), 887–890 (2016).
17. M. Kutila, P. Pyykönen, H. Holzhüter, M. Colomb, and P. Duthon, "Automotive LiDAR performance verification in fog and rain," in *2018 21st International Conference on Intelligent Transportation Systems (ITSC)*, (2018), pp. 1695–1701.
18. L. Zhang, Y. Li, Y. Hou, Y. Wang, M. Tao, B. Chen, Q. Na, Y. Li, Z. Zhi, X. Liu, X. Li, F. Gao, X. Luo, G.-Q. Lo, and J. Song, "Investigation and demonstration of a high-power handling and large-range steering optical phased array chip," Opt. Express **29**(19), 29755–29765 (2021).
19. R. Baets, A. Subramanian, S. Clemmen, B. Kuyken, and S. Severi, "Silicon photonics Silicon nitride versus silicon-on-insulator," in *Optical Fiber Communication Conference, OSA Technical Digest (online)* (Optical Society of America, 2016), paper Th3J.1.
20. C. V. Poulton, M. J. Byrd, M. Raval, Z. Su, N. Li, E. Timurdogan, D. Coolbaugh, D. Vermeulen, and M. R. Watts, "Large-scale silicon nitride nanophotonic phased arrays at infrared and visible wavelengths," Opt. Lett. **42**(1), 21–24 (2017).
21. C.-S. Im, B. Bhandari, K.-P. Lee, S.-M. Kim, M.-C. Oh, and S.-S. Lee, "Silicon nitride optical phased array based on a grating antenna enabling wavelength-tuned beam steering," Opt. Express **28**(3), 3270–3279 (2020).
22. N. A. Tyler, D. Fowler, S. Malhouitre, S. Garcia, P. Grosse, W. Rabaud, and B. Szelag, "SiN integrated optical phased arrays for two-dimensional beam steering at a single near-infrared wavelength," Opt. Express **27**(4), 5851–5858 (2019).
23. P. Wang, G. Luo, Y. Xu, Y. Li, Y. Su, J. Ma, R. Wang, Z. Yang, X. Zhou, Y. Zhang, and J. Pan, "Design and fabrication of a SiN-Si dual-layer optical phased array chip," Photonics Res. **8**(6), 912–919 (2020).
24. Q. Wang, S. Wang, Y. Zeng, W. Wang, Y. Cai, Z. Tu, W. Yue, X. Wang, Q. Fang, and M. Yu, "Dual-layer waveguide grating antenna with high directionality for optical phased arrays," Appl. Opt. **58**(21), 5807–5811 (2019).
25. W. D. Sacher, Y. Huang, G.-Q. Lo, and J. K. S. Poon, "Multilayer Silicon Nitride-on-Silicon Integrated Photonic Platforms and Devices," J. Lightwave Technol. **33**(4), 901–910 (2015).
26. J. H. Kim, J. B. You, J. H. Park, K. Yu, and H. H. Park, "Design of nano-photonic phased-array antennas for wide-angle beam-steering," in *International Conference on Advanced Communication Technology*, (2016), pp. 422–425.
27. L. Zhang, Y. Li, M. Tao, Y. Wang, Y. Hou, B. Chen, Y. Li, L. Qin, F. Gao, X. Luo, G. Lo, and J. Song, "Large-scale integrated multi-lines optical phased array chip," IEEE Photonics J. **12**, 1–8 (2020).